Raman and Near-Infrared Spectroscopy of Candidate X-Ray Amorphous Phases in Martian Rocks and Soils: Implications for Mars 2020 and ExoMars 2020 Data

Gregerson, J. C.[1], A. D. Rogers[1*], L. Ehm[1], E. C. Sklute[2], and J. B. Parise[1]

[1]Stony Brook University, 255 Earth and Space Sciences Bldg., Stony Brook, NY 11794-2100
[2]Planetary Science Institute, 1700 E. Fort Lowell Rd Suite 106, Tucson, AZ 85719

*Corresponding author: deanne.rogers@stonybrook.edu

To be submitted to *Earth and Space Science*

Abstract

Martian soils and rocks contain a significant fraction of amorphous materials, based on previous lander-based x-ray diffraction and orbital infrared measurements. However, the exact nature and chemistry of the phases that make up this component are not well constrained. The upcoming Mars2020 and ExoMars rovers will carry Raman and visible/near-infrared (VNIR) reflectance spectrometers, offering new methods for characterizing Martian surface materials in-situ. Raman spectroscopy in particular has the potential to discriminate between amorphous phases; however, many of the candidate amorphous phases are absent from Raman spectral databases. We synthesized and spectrally characterized candidate x-ray amorphous phases for Martian soils (amorphous ferric sulfate, allophane, ferrihydrite, allophane with adsorbed sulfate and phosphate, and ferrihydrite with adsorbed sulfate and phosphate) with Raman and VNIR spectroscopy and document the Raman peak locations for these materials. We found that sulfate and phosphate anions were Raman-detectable when adsorbed to allophane, but were not observed when adsorbed to ferrihydrite; a possible cause for this includes decomposition of the adsorbed species during the Raman acquisition. We show that candidate sulfur-bearing species -- amorphous ferric sulfate and allophane with adsorbed sulfate -- are distinguishable in Raman data. Allophane, ferrihydrite and amorphous ferric sulfate exhibit distinctive VNIR spectra, but are not likely to be distinguishable in the VNIR if mixed with other materials. The potential for detecting adsorbed species is a unique strength of Raman spectroscopy compared to other spectral methods, however further studies are needed to understand the acquisition conditions, abundances and matrix compositions under which adsorbed species can be detected.

Plain Language Summary

Martian sediments consist of a mixture of rock fragments, minerals, and other materials that lack a well-defined crystalline structure ("x-ray amorphous" materials). The nature and species of the x-ray amorphous materials has not been determined using instrumentation from currently active or past missions. Upcoming rover missions will carry a different kind of instrumentation (Raman spectrometers) that are very commonly used in terrestrial laboratories but that have never before been brought to Mars. We measured some of the candidate amorphous materials using this instrumentation and show that they can be distinguished from one another. We documented the diagnostic Raman features of these materials, for comparison to data that will be returned from future missions. Knowing which species are present is important for understanding the origin of Martian rocks and soils, as well as for understanding the potential changes over time that rocks and soils may experience due to burial or interaction with later fluids.

1. Introduction

Amorphous and nanocrystalline materials have been shown to constitute a significant portion of Martian surface materials from both rover-based in-situ X-ray diffraction measurements as well as from landed and orbital spectroscopic measurements. Using data from the CheMin X-ray diffractometer instrument, the Mars Science Laboratory (MSL) science team has inferred that up to 70 wt% of rocks and 50 wt% of soils in Gale crater contain "X-ray amorphous" material (Bish et al. 2013; Blake et al. 2013; Dehouck et al. 2014; Vaniman et al. 2014; Rampe et al., 2017; Achilles et al. 2020; Rampe et al. 2020). "X-ray amorphous" implies material that lacks the long-range atomic ordering necessary to exhibit Bragg peaks in X-ray diffraction patterns, and can include a range of amorphous materials, like glasses, or poorly-/nano-crystalline phases. Using supplemental chemical data from the Alpha Particle X-ray Spectrometer (APXS) instrument and evolved gas analysis (EGA) data from the Sample Analysis at Mars (SAM) instrument suite on MSL, the X-ray amorphous fraction likely consists of multiple phases. Potential materials include silicate glass, allophane, nanophase iron oxides, amorphous salts, and other poorly crystalline weathering products; however, despite the constraints on chemistry, it is unknown what combination of phases make up the X-ray amorphous fraction of Martian rocks and soils. Amorphous materials have also been inferred spectroscopically from orbit and ground and are likely dominated by various forms of amorphous silicate (e.g., glass/altered glass, amorphous

silica, allophane, imogolite) and ferric oxides (e.g. Bell et al., 1993 Bandfield, 2002; Michalski et al., 2005; Glotch et al., 2006; Milliken et al., 2008; Ruff et al., 2011; Horgan and Bell, 2012; Rampe et al., 2012; Farrand et al., 2016; Cannon et al., 2017).

Of particular interest to this study is the nature of the sulfur-bearing amorphous component(s). Relative to the crystalline fraction of Gale soils, the amorphous fraction is enriched in iron, sulfur and H_2O, with ~3-6 wt% water (Bish et al. 2013; Dehouck et al. 2014; Leshin et al. 2013; McAdam et al. 2014). Proposed sulfur-bearing amorphous phases include amorphous sulfates (Dehouck et al., 2014; McAdam et al., 2014; Sklute et al., 2015) and/or chemisorbed sulfate anions onto nanocrystalline weathering products such as ferrihydrite or allophane (Dehouck et al., 2014; McAdam et al., 2014; Rampe et al., 2016). Amorphous iron sulfates have been shown to form by path dependent dehydration from concentrated brines or crystalline sulfate hydrates, and thus could potentially form under certain Martian conditions (e.g. Xu et al., 2009; Wang et al., 2012; Sklute et al., 2015). Nanophase minerals and mineraloids including ferrihydrite and allophane are common immature weathering products in terrestrial basalts and volcanic soils. These nanophase materials can collect ions such as sulfate and phosphate with their hydroxylated surfaces and large amount of surface area (e.g. Wada, 1987; Rampe et al., 2016).

Just like crystalline minerals, amorphous species are tracers of environmental conditions, during formation, diagenesis, and later episodes of alteration. Thus it is critically important to identify and distinguish between these species. For example, allophane, imogolite and hisingerite are common immature products of silicate weathering (particularly in ashy/glassy protoliths) (e.g. Wada, 1987; Dahlgren et al. 2004; Bishop et al. 2013). Thus identification of these phases could signify water-limited alteration and/or a higher proportion of glass in the protolith material. For another example, take the sulfur-bearing components described above. The presence of amorphous Mg, Fe(II) or Fe(III) sulfate phases, which form from rapid brine evaporation or dehydration of crystalline sulfates, depending on the cation (e.g. Vaniman et al., 2004; Xu et al., 2009; Sklute et al., 2015), could indicate acid sulfate weathering conditions and/or an evaporative process. But, if the sulfur instead arises from chemisorbed sulfate anions on nanophase silicate weathering products (e.g. allophane/ferrihydrite), this could indicate circum-neutral water-limited alteration with later exposure to sulfur-bearing fluids (e.g. Wada, 1987; Rampe et al., 2016). Last, amorphous phases can be indicators of aqueous activity after formation. For example, ferrihydrite is relatively unstable on Earth and rapidly transforms to

hematite or goethite upon exposure to aqueous solutions. However, its fate does depend on fluid:rock ratio, temperature, and solution chemistry (Dehouck et al. 2017). For example, low fluid:rock ratio (Dehouck et al., 2017), as well as the presence of chemisorbed PO_4^{3-} on ferrihydrite (Galvez et al., 1999) have both been shown to inhibit the transformation of ferrihydrite to other iron oxides. However, exposure to high temperatures, such as through burial, would likely preclude the preservation of ferrihydrite (e.g. Dehouck et al., 2017).

A potential method to distinguish between candidate X-ray amorphous phases is to use Raman spectroscopy. Raman spectrometers will be sent to surface of Mars via both the Mars 2020 rover mission and the ExoMars 2022 rover mission. Mars 2020 will carry the SuperCam instrument, which includes a remote, time-resolved Raman spectrometer that uses a 532 nm excitation laser (Weins et al., 2017) and the SHERLOC instrument, which includes a microimaging Raman spectrometer with a 248 nm excitation laser (Beegle et al., 2015). The ExoMars rover will include a Raman spectrometer with a 532 nm excitation laser, to analyze drilled and powdered samples at close range within the rover body (Rull et al., 2017). Additionally, both rovers will carry near-infrared (NIR) reflectance spectrometers (Wiens et al., 2017; Bibring et al., 2017) that may also provide supporting characterization of amorphous components. For example, differences in NIR band shape and position are observed between amorphous sulfates and silicate weathering products (e.g. Sklute et al., 2015; Rice et al., 2013; Bishop et al., 2013); however, some amorphous samples are not well distinguished from crystalline hydrated samples (e.g. amorphous Mg sulfate vs Mg hexahydrite, Wang et al., 2009). Nevertheless, the accompanying NIR data could help to distinguish between some species.

An extensive literature review has shown that, with the exception of nanophase iron (oxyhydr)oxides (e.g. Das and Hendry, 2011; Sklute et al., 2018) and amorphous ferric sulfate (Ling and Wang, 2010; Wang et al., 2012), Raman characterizations are absent for many of the proposed x-ray amorphous phases. Additionally, though Raman characterization of amorphous ferric sulfate has been presented previously (e.g. Ling and Wang, 2010), those phases are not publicly available. In this work, we characterize and compare Raman and visible/near-infrared (VNIR) spectra of a selection of candidate x-ray amorphous phases: synthetic amorphous ferric sulfate ($Fe_2(SO_4)_3 \cdot$~6-8H_2O), allophane (1.0-2.0$SiO_2 \cdot Al_2O_3 \cdot$2.5-3.0$H_2O$), ferrihydrite ($5Fe_2O_3 \cdot$~9$H_2O$), and allophane and ferrihydrite with chemisorbed sulfate and phosphate (**Table 1**). The samples with chemisorbed phosphate were included in our study because the amorphous

component of Gale soils also includes minor phosphate, and additionally, phosphate is commonly chemisorbed on terrestrial volcanic soils (e.g. Rampe et al., 2016). Our spectra could help these phases to be identified or ruled out based on returned data from the upcoming rover missions, and might be used to test hypotheses regarding the sulfur-bearing amorphous component in Martian soils and rocks.

2. Materials and Methods

2.1 Sample synthesis

2.1.1 Amorphous ferric sulfate. allophane, and ferrihydrite synthesis

Anhydrous $Fe_2(SO_4)_3$ (99.998% purity) was deliquesced in a 99% RH environment buffered by deionized water to form a solution with a concentration of 32.3wt% $Fe_2(SO_4)_3$. This solution was dehydrated via vacuum for seven days to form an amorphous solid as per Sklute et al. (2015).

Synthesis of allophane was adapted from Ohashi et al. (2002). 0.1 M solutions of $AlCl_3$ and Na_4SiO_4 were prepared by dissolving reagents (99% and 99.5% purity, respectively) in deionized water. Solutions were combined at a ratio of Si/Al = 0.75 and stirred for 1h. The resulting mixture was centrifuged for 30 minutes at 6000 rpm to separate the allophane precursor gel from the saline supernatant. The precursor was then placed in an autoclave at 100 °C for 48 hours. The solids were washed with deionized water and then separated by centrifuge three times and then dried at 40 °C overnight. Solids were ground with an agate mortar and pestle.

Synthesis of two-line ferrihydrite was adapted from Schwertmann and Cornell (2000). 40 g of $Fe(NO_3)*9H_2O$ (reagent) was dissolved in 500 mL of deionized water and then brought to a pH of 7.15 using 1 M KOH. The mixture was stirred for 24 hours and centrifuged for 30 minutes at 6000 rpm to separate the solids from the supernatant. Solids were washed with deionized water and centrifuged three times and then dried at 40 °C overnight. Solids were ground with an agate mortar and pestle.

2.1.2 Adsorption of Sulfate and Phosphate

Methods for sulfate and phosphate adsorption onto the surface of allophane and ferrihydrite were adapted from Rampe et al. (2016). For all sulfate and phosphate solutions, a background solution

of 0.1 M KCl was made by dissolving KCl (reagent) in deionized water.

For allophane, 0.015 M solutions of K_2SO_4 and K_2HPO_4 were prepared by adding solid K_2SO_4 and K_2HPO_4 (reagents) to the 0.1 M KCl background solutions. The pH of each solution was adjusted to 5.84 (sulfate solution) and 5.53 (phosphate solution) using HCl and KOH (reagents). 0.6164 g of allophane was added to 45 mL of this sulfate solution and 0.6235 g of allophane was added to 45 mL of this phosphate solution. Each was then stirred for 24 h before being centrifuged for 30 minutes at 6000 rpm to separate the solids from the supernatant. Solids were washed with deionized water and centrifuged three times and then dried at 40 °C overnight. Samples were ground with an agate mortar and pestle for sample analysis.

For ferrihydrite, 0.015 M solutions of K_2SO_4 and Na_2HPO_4 were prepared by adding solid K_2SO_4 and Na_2HPO_4 (reagents) to the 0.1 M KCl background solutions. The pH of each solution was adjusted to 4.18 (sulfate solution) and 4.11 (phosphate solution) using HCl and NaOH (reagents). 1.2009 g of ferrihydrite was added to 90 mL of this sulfate solution and 1.2008 g of ferrihydrite was added to 90 mL of this phosphate solution. Each was then stirred for 24 h before being centrifuged for 30 minutes at 6000 rpm to separate the solids from the supernatant. Solids were washed with deionized water and centrifuged three times and then dried at 40 °C overnight. Samples were ground with an agate mortar and pestle for sample analysis.

2.2 Sample Analysis

2.2.1 Chemical analysis

We used thermogravimetric analysis (TGA) to determine the water content of allophane and ferrihydrite. The instrument used is a Netzsch STA 449 C. For amorphous ferric sulfate, weight percent of water was determined by mass loss from dehydration. We determined the amount of water by weight percent by mass loss from heating for allophane and ferrihydrite.

We determined the chemistry of each allophane and ferrihydrite sample using inductively coupled plasma optical emission spectrometry (ICP-OES). A small amount of each sample was dissolved in 10% HNO_3 for chemical analysis. Reference solutions were also prepared in 10% HNO_3 for each element analyzed. The reference and sample solutions were analyzed using a Thermo iCAP 6300 radial view inductively coupled plasma-atomic emission spectrometer. The

Thermo Scientific iTEVA software was used to produce final concentrations from the data.

2.2.2 X-ray Diffraction

X-ray diffraction (XRD) was used to confirm the amorphous nature and/or the phase identity of the synthetic amorphous ferric sulfate, allophane, and ferrihydrite samples. XRD measurements were carried out on two instruments: (1) a Rigaku Miniflex (15 mA; 40 kV; 0.02 °/step; 0.40 s/step) with a Cu Kα radiation source, and using a quartz zero-background sample holder, and (2) an Olympus BTX-II (30 kV, 0.05 2θ, 64 exposures) with a Co Kα radiation source using a Kapton sample holder. The BTX-II was used for a more direct comparison to diffraction patterns taken by CheMin whereas the Miniflex offered a wider range of scattering vector (Q) values for better phase identification.

2.2.3 Raman Spectroscopy

All samples were examined and characterized using continuous wave Raman spectroscopy. Raman spectra were acquired using three different excitation wavelengths (UV: 325 nm, green: 532nm, and red: 785 nm) to compare the Raman response for each material as a function of excitation energy. Peak locations were determined by finding the intensity maxima after smoothing with a 5-channel boxcar filter.

The green laser Raman setup is a WiTEC alpha300R confocal Raman microscope system equipped with a 532 nm Nd:YAG excitation laser. Spectra were acquired at 7 mW power (P) with 120 accumulations of 10 second exposures under 20x magnification (~1.6 μm laser spot size, d). Under these conditions, we estimate a power density of ~3.5 mW / μm^2, using the following equation (Xi et al., 2019):

$$D = 4P / (\pi d^2) \quad (1)$$

The 532 nm laser excitation wavelength matches that of the upcoming Mars 2020 rover SuperCam Raman subsystem (Wiens et al., 2017) as well as the Raman spectrometer on the ExoMars 2020 rover (Rull et al., 2017).

For amorphous ferric sulfates, additional Raman spectra were acquired with a B&W Tek iRamanPlus portable spectrometer using a 532 nm laser, under 50mW power for 30-120 s, under

a nitrogen-purged atmosphere to prevent hydration or deliquescence. The additional 532 nm Raman measurements were done to evaluate any spectral changes with instrument setup as well as any potential changes with exposure to humidity.

All samples were characterized using two additional laser excitation wavelengths, 785 nm and 325 nm. These measurements were taken using a Renishaw InVia confocal Raman microscope, using 5x magnification, 100 mW (UV) and 320 mW (red) power and ten, 10-second exposures. Estimated spot sizes and power densities for the UV and red acquisitions are ~3 μm / ~12.0 mW/μm^2 and ~8 μm / ~6.4 mW/ μm^2, respectively, using equation (1). These additional spectra were acquired in order to characterize any spectral changes with excitation laser wavelength. The 325 nm laser is closer to the laser wavelength of the micro-Raman spectrometer on the SHERLOC (Scanning Habitable Environments with Raman & Luminescence for Organics & Chemicals) instrument on Mars 2020 (248 nm, Beegle et al., 2015), but likely more susceptible to fluorescence than the deep UV range of SHERLOC (e.g. Tarcea et al., 2007).

All Raman spectra were baseline-corrected with a "rubberband" correction (Warterwig, 2003; Dyar et al., 2016) using the Mt. Holyoke College DEVAS web interface, using parameters of 12 iterations and over a range of 64 channels (Carey et al., 2017). Rare noise spikes due to galactic cosmic rays were manually removed from the baseline-corrected spectra. Finally, spectra were then smoothed using a 5-channel boxcar filter. Uncorrected Raman data, as well as filtered and baseline-corrected data are included in the data repository.

2.2.4 Visible/Near-Infrared Reflectance (VNIR)

Visible/near-infrared reflectance (VNIR) spectra (350-2500 nm) were collected for allophane and ferrihydrite samples with an ASD Fieldspec3 spectrometer using incidence and emergence angles of 30° and 0°, respectively, and measured relative to Spectralon. VNIR spectra of amorphous ferric sulfate were previously presented by Sklute et al. (2015) and were not re-acquired in this study.

3. Results

3.1 Chemistry and hydration

Table 1 shows the chemical information of allophane and ferrihydrite samples obtained using ICP-OES. This includes wt% of adsorbants and Si/Al atomic ratio for allophane as well as water contents for amorphous ferric sulfate, allophane, and ferrihydrite.

Table 1. Sample Compositions

Sample	Water Content (wt %)	Adsorbant	Si/Al
Amorphous Ferric Sulfate	22.3		
Allophane	26.7		0.59
Allophane + SO_4		4.2 wt% SO_4	0.58
Allophane + PO_4		8.7 wt% PO_4	0.57
Ferrihydrite	22.0		
Ferrihydrite + SO_4		2.9 wt% SO_4	
Ferrihydrite + PO_4		8.3 wt% PO_4	

3.2 X-ray Diffraction

X-ray diffraction (XRD) data from the Miniflex for all samples are shown in **Figure 1**. Our sample of amorphous ferric sulfate does not exhibit any sharp Bragg peaks, and shows only a broad diffraction pattern peaking at 25 2θ, consistent with Sklute et al. (2015). Allophane shows broad, diffuse peaks centered at 2θ values of 29, 42 and 68. These peaks correspond to the allophane d-spacing features at 1.4, 2.2, and 3.4 Å, consistent with those reported by Ohashi et al. **(**2002**)** and Rampe et al. (2016). The allophane features did not change position or shape with the addition of adsorbed ions, confirming that the allophane crystal structure is constant throughout the adsorption experiments. Ferrihydrite shows broad diffuse peaks at 2θ values of 36 and 65. These peaks correspond to ferrihydrite d-spacing features at 1.5 and 2.6 Å, consistent with those reported by Schwertmann and Cornell (2000) and Rampe et al. (2016). As with allophane, the structure of ferrihydrite was preserved throughout the adsorption experiments.

Diffraction patterns acquired with the BTX-II are shown in **Figure S1**; no significant differences in broad peak locations were observed between instruments, once adjusted for differences in radiation source (Co vs Cu). However, the amorphous ferric sulfate XRD pattern acquired with the BTX-II is more similar to a previously published pattern (Sklute et al., 2015) than that acquired with the Miniflex. Nevertheless, both instruments confirm the x-ray amorphous nature of the sample.

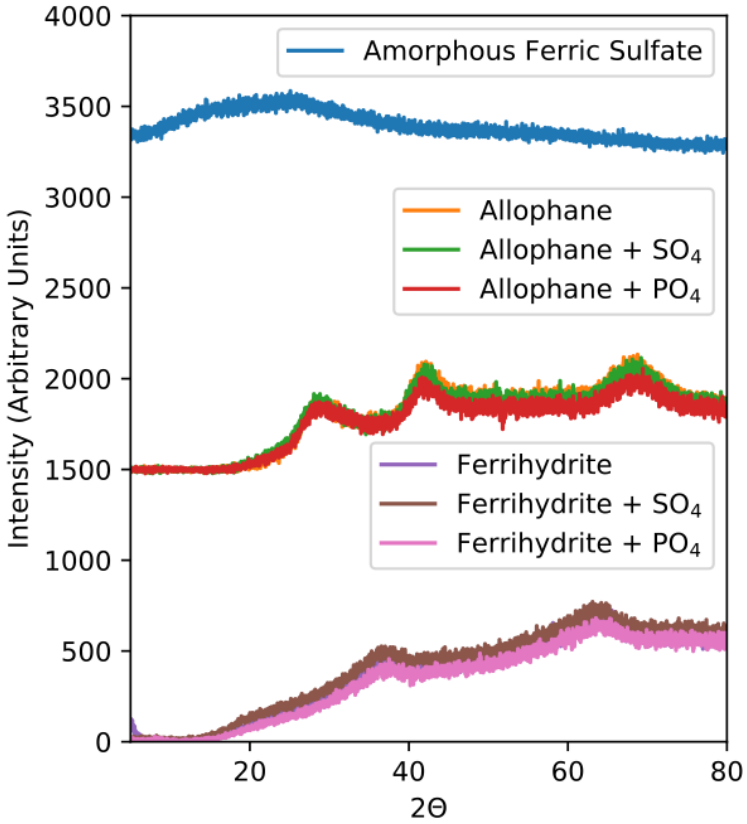

Figure 1. Miniflex XRD Data for all samples. Diffraction patterns are offset with all allophane and ferrihydrite superposed to emphasize the lack of change in diffraction pattern from adsorption**.**

3.3 Raman Spectroscopy

Raman spectra for all phases, grouped by excitation energy, are shown in **Figure 2. Table 2** shows the observed Raman modes of all materials examined in this study as well as those of related materials from previous studies.

For each sample, Raman spectra collected from each excitation energy (UV, green, red) show differences in peak location, magnitude, and shape (**Figure 2**, **Table 2**). In some cases, Raman

peaks are present in one excitation energy but absent in another; for example, the 1356 cm^{-1} peak in allophane is only present in the 785 nm laser data. The biggest differences observed across excitation energies was for the ferrihydrite samples. As will be described in more detail below, these large differences are due to a phase transformation that occurred during the 532 nm Raman data acquisition, and probably also during the 325 nm acquisition.

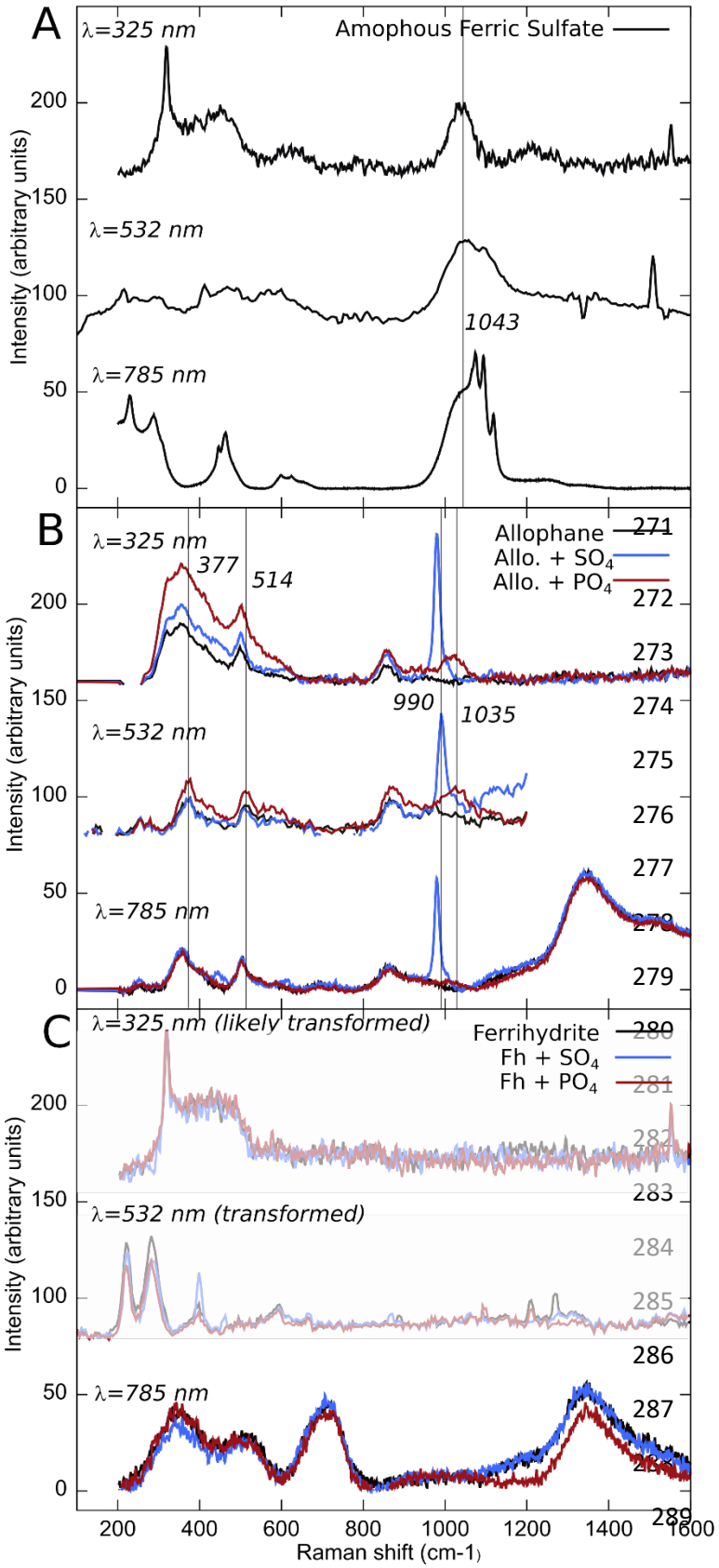

Figure 2. Raman spectra acquired of amorphous ferric sulfate (A), allophane with and without adsorbants (B), and ferrihydrite with and without adsorbants (C). The ferrihydrite samples acquired at higher energies likely transformed during acquisition; see text. Vertical lines highlight peaks of interest shown in the 532 nm data.

Table 2. Raman modes for the X-ray amorphous materials examined in this study and for related materials.

Phase of Interest	Excitation (λ, nm)	H_2O		SO_4				PO_4				SiO_2					Other peaks	Ref.
		Stretch	Bend	ν_1	ν_2	ν_3	ν_4	ν_1	ν_2	ν_3	ν_4							
SO_4	532	-	-	983	450	1105	611											2
PO_4	532							938	420	1017	567							3
$Fe_2(SO_4)_3 \cdot 5H_2O$	532	3057 3195 3323 3425	1605 1653	1017 1036 1051	416 441 457 468 494	1087 1119 1189	599 614 631 652										253 281	4
$Al_2(SO_4)_3 \cdot 17H_2O$	532	3246		992	470	1086 1126	612										309	8
Am. Ferric Sulfate	325			**1047**	**(450)**	**1214**	**623**											1
	532	3180 3398 3521	1634	993 1035	424 472	1089 1231	598 628 660										199 277	4
	532			**1045**	**508**												**361 707**	1
	785			**1074**	**463**		**624**											1
α-Quartz	532											373	512	780	1150			5
Allophane	325											**336**	**500**	**862**				1
	532											**377**	**520**	**873**				1
	785											**359**	**503**	**865**			**1356 (1527)**	1
Allo + SO_4	325			**980**			**618**					**336**	**500**	**862**				1
	532			**990**								**377**	**520**	**873**				1
	325			**980**	**447**	**1126**	**617**					**359**	**503**	**865**			**1356 (1527)**	1
Allo + PO_4	325									**1026**		**336**	**500**	**862**				1
	532									**1025**		**377**	**520**	**873**				1
	785									**1026**		**359**	**503**	**865**			**1356 (1527)**	1
		H_2O		SO_4				PO_4						Ferrihydrite				
		Stretch	Bend	ν_1	ν_2	ν_3	ν_4	ν_1	ν_2	ν_3	ν_4	Hematite						
Ferrihydrite	*325**												***320***	***445***				**1552**	1
	532													370	510	710			6
	*532**											***282***	***398***		***595***				1
	785													361	508	707	1045		7
	785													**355**	**504**	**714**		**1352**	1
Fh + SO_4	*325**												***320***	***(445)***				***1552***	1
	*532**											***282***	***398***		***595***				1
	785													**344**	**504**	**706**		**1352**	1
Fh + PO_4	*325**											***320***	***445***					***1552***	1
	*532**											***282***	***398***		***595***				1
	785													**344**	**504**	**706**		**1353**	1
Hematite	532											290-300	412						6
	785											290	408	490	607				7

Italics* : Indicates phase likely underwent transformation during measurement. (Parentheses): indicates very broad or weak feature, in some cases likely due to flourescence. References: **1-- this study; 2--Ross (1974a); 3--Ross (1974b); 4--Ling and Wang (2010); 5--Moenke (1971); 6--Hanesch (2009); 7--Das and Hendry (2011); 8--Wang and Zhou (2014)

3.3.1 Samples without adsorbants

In the amorphous ferric sulfate sample, the most distinctive peak is observed at 1045-1074 cm^{-1} (**Figure 2**), due to the SO_4^{2-} ν_1 fundamental mode (**Table 2**). Other major peaks can be identified below 600 cm^{-1}; these vary slightly depending on excitation energy. Though the sample is hydrated, Raman features due to hydration are not apparent. The ν_1 mode location is similar in position to hydrated crystalline ferric sulfate (**Table 2**); however, the peak is significantly broadened in the amorphous phase (Ling and Wang, 2010). In the data acquired with the 785 nm excitation, three sharp narrow peaks are superimposed on the broad ν_1 feature, suggesting that the sample may have undergone partial crystallization before measurement.

Allophane shows peaks at ~360, ~510, and 870 cm^{-1}, taking the average of the peak centers from each excitation energy (**Figure 2, Table 2**). These peaks are similar to those reported by Coccato et al. (2016) for a purported sample of allophane (no sample characterization was reported) at 364, 502, and 858 cm^{-1}. In the 532 nm Raman data, there is also a large broad feature centered at about 1666 cm^{-1} that spans from ~1200 to ~2600 cm^{-1}; this is likely a fluorescence affect. With the 785 nm laser, a broad feature at 1527 cm^{-1} is present, and is superposed by a narrower peak at ~1356 cm^{-1}. We were unable to attribute that feature to a particular molecular group, however we note that it is present in both our allophane and ferrihydrite samples (**Figure 2**), and is also common in other iron oxides (Hanesch, 2009) (**Figure 3**) and carbon-bearing species. We do not consider the ~1356 cm^{-1} peak to be diagnostic of either of these phases.

The spectra of ferrihydrite are variable with excitation energy. Those taken with the 532 nm laser show peaks at Raman Shift values of 282, 398, and 595 cm^{-1}. These peaks are inconsistent with previously reported values for ferrihydrite (Hanesch, 2009; Sklute et al., 2018), but rather closely resemble those of hematite (Hanesch, 2009; Sklute et al., 2018) (**Figure 3, Table 2)**. This suggests that all three of our ferrihydrite samples were transformed into hematite from exposure to the 532 nm laser. We were unable to obtain a ferrihydrite signal using lower laser power and longer integration times. This is discussed further in **Section 4**. The spectra acquired with the 325 nm excitation energy generally lack features except for a sharp peak at 320 cm^{-1} and broad hump at 445 cm^{-1}. These features generally match those of the amorphous ferric sulfate sample, with the exception of the 1047 cm^{-1} peak in the amorphous ferric sulfate. It is unclear whether

the ferrihydrite sample also experienced transformation; however, because of the higher power density associated with our UV measurements, we would expect the sample to have converted, as with the green laser.

Our ferrihydrite samples measured with the 785 nm laser match closely with those previously reported by Das and Hendry (2011) and Sklute et al. (2018), indicating little-to-no transformation during measurement (**Figure 3**). These spectra exhibit broad peaks at Raman shifts of 355, 504 and 714 and 1352 cm^{-1}. The first three of these peaks are likely ferrihydrite peaks, which have been reported at 361, 508, and 707 cm^{-1} for this laser wavelength (Das and Hendry, 2011). Das and Hendry did not present spectra above 1200 cm^{-1}. We note that maghemite and ferrihydrite are spectrally similar (Sklute et al., 2018), and that our ferrihydrite sample may have minor amounts of maghemite based on the minor dip at 430 cm^{-1} (see also **Section 4.1**).

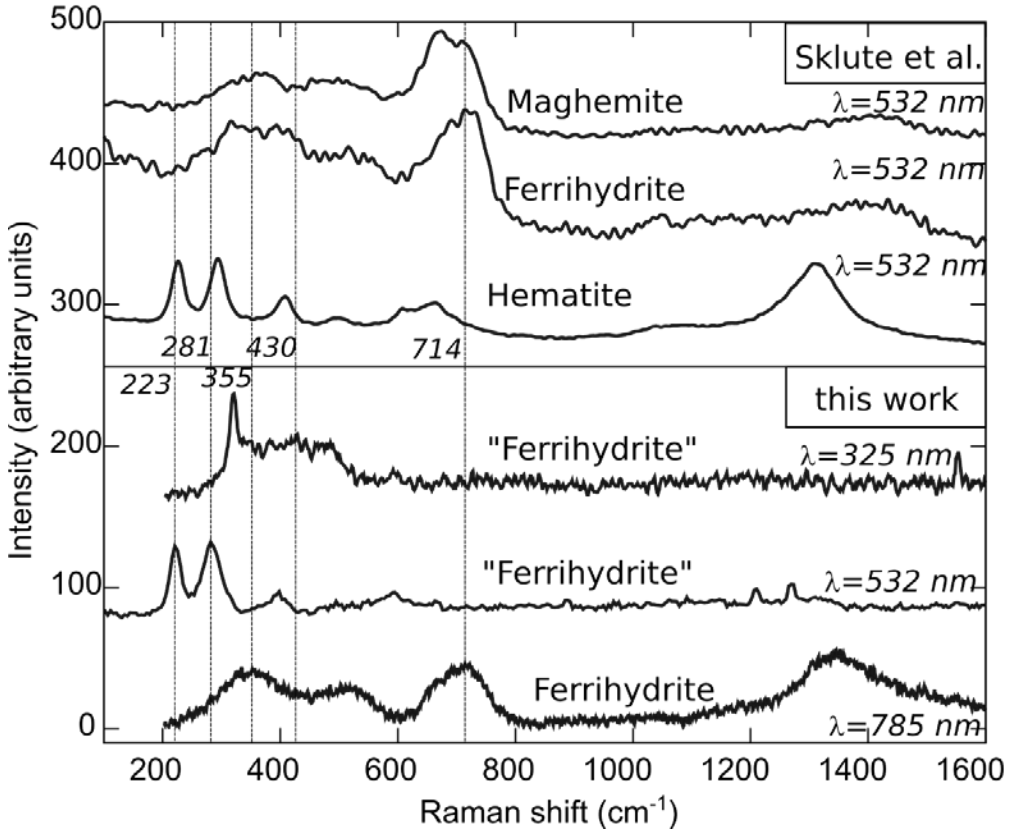

Figure 3. Comparison of our ferrihydrite samples with ferrihydrite and hematite spectra from Sklute et al., (2018), who used much lower laser power and longer integration times. Our sample measured using a 532nm excitation exhibits peaks consistent with hematite. Our sample

341 measured using 785 nm excitation is consistent with ferrihydrite, with possibly minor amounts of
342 maghemite. The sample measured using 325 nm excitation is not consistent with either
343 ferrihydrite, magnetite, or hematite.

344

345 **3.3.2 Samples with adsorbants**

346 In all three excitation energies, allophane with adsorbed sulfate shows a sharp peak at 980-990
347 cm^{-1}, consistent with sulfate (Ross, 1974a). The absorbed sulfate peak is clearly shifted to lower
348 frequencies than that of the broad sulfate peak associated with amorphous ferric sulfate (**Figure**
349 **2**). We note that the adsorbed sulfate peak position (990 cm^{-1}, λ=532nm) is nearly identical to the
350 ν_1 sulfate peak in crystalline aluminum sulfate (992 cm^{-1}, λ=532nm) (Wang and Zhou, 2014)
351 (**Table 2**); however, aluminum sulfate also contains clear ν_4 and ν_2 peaks at ~612 and ~470 cm^{-1}
352 that would permit its distinction from allophane with adsorbed sulfate complexes. Allophane
353 with adsorbed phosphate shows a somewhat broad peak at ~1025 cm^{-1} in all three excitation
354 energies consistent with phosphate (Ross, 1974b); however, the 1025 cm^{-1} feature is very weak
355 in the 785 nm data (**Figures 2,3; Table 2**).

356 In contrast with allophane, no evidence of adsorbed sulfate anions are observed in the
357 ferrihydrite Raman data, and only a very weak hump near ~1025 cm^{-1} is present in the
358 phosphate-bearing ferrihydrite sample in the red laser acquisitions. Potential causes for the lack
359 of detection are discussed in **Section 4.1**.

360 **3.4 Visible / Near Infrared (VNIR) Spectroscopy**

361 Allophane reflectance spectra (**Figure 4**) exhibit a blue slope, with greater reflectance at shorter
362 wavelengths. Spectral features are observed at 970, 1160, 1438, 1940, and 2209 nm, with little to
363 no observable differences between allophane and allophane with adsorbed sulfate and phosphate,
364 except for an increase in overall reflectance. The ferrihydrite reflectance spectra show
365 absorptions at 1437 and 1934 nm, due to H_2O vibrational overtones and combinations. Similar to
366 allophane, ferrihydrite with adsorbed sulfate and phosphate does not exhibit any additional
367 features, but shows a greater reflectance with adsorbed sulfate and phosphate. These findings are
368 consistent with those presented by Rampe et al. (2016).

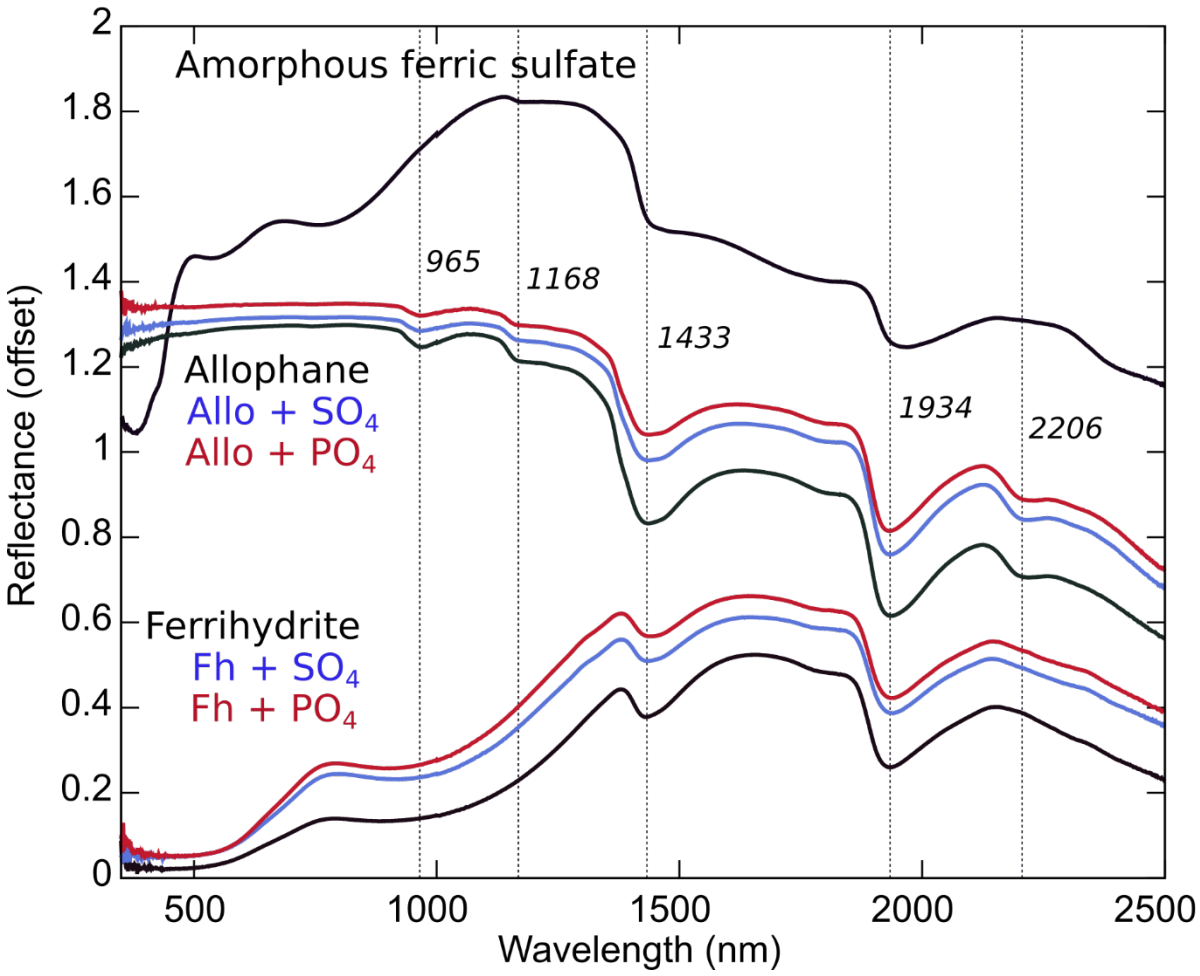

Figure 4. VNIR reflectance spectra of allophane and allophane with adsorbed sulfate and phosphate. Amorphous ferric sulfate from Sklute et al., (2015) is shown for comparison. Allophane spectra are offset from ferrihydrite spectra by 0.35; amorphous ferric sulfate is offset from ferrihydrite spectra by 1.0. Vertical lines designate features observed in allophane and permit easier comparison of feature positions between all samples.

4. Discussion

4.1 Lack of detection of adsorbed species on ferrihydrite

Unlike our allophane samples, SO_4^{2-} was not detected in Raman spectra when adsorbed to ferrihydrite, and PO_4^{3-} was barely discernible in only one excitation energy (**Figure 2, Section 3.3**). The lack of detection suggests that either the adsorbed phases are somehow obscured in the sample, or that they were lost either before or during the measurement. We note that our ICP data confirms the presence of the sulfate and phosphate anions, and also that these samples showed a noticeable brightening in the VNIR data. Both of these observations indicate that the adsorbed phases were indeed present in the samples and that the samples were visibly changed by the adsorption process. Thus, we suggest that the sulfate anions, and much of the phosphate anions, may have been volatilized during the Raman acquisitions of ferrihydrite. Evolved gas analyses (EGA) of ferrihydrite and allophane samples (with and without adsorbed species) by Rampe et al. (2016) showed evolved SO_2 peaks at ~400, 490, and 700 °C in their ferrihydrite + adsorbed sulfate sample, indicating that adsorbed SO_4^{2-} begins to decompose at temperatures as low as ~400 °C. The temperature at which ferrihydrite dehydrates and transforms to hematite, when containing adsorbed sulfate, was suggested to occur at 440 °C, again based on EGA measurements of evolved H_2O (Rampe et al., 2016). Given that we observed a hematite transformation in our 532 nm Raman data, this suggests that our sample was likely heated to a temperature that decomposed the adsorbed SO_4^{2-}.

As for the 785 nm Raman acquisitions, we suggest that the ferrihydrite sample may also have experienced enough heating to remove all of the SO_4^{2-} and much of the PO_4^{3-} (phosphate discussed below). Our spectra were acquired with a power density of ~6.4 mW / μm^2. Previous work by Novak et al. (2016), who modeled the laser-induced heating of amorphous silicon films, showed that temperatures would exceed ~400 °C for power densities of ~5 mW/ μm^2 or greater. These temperatures would likely be even higher for our dark, iron-bearing samples. Thus, we conclude that it is plausible that adsorbed sulfate was lost from ferrihydrite during our Raman acquisitions. Finally, we note that ferrihydrite is spectrally similar to maghemite in Raman data (Sklute et al., 2018), and that our ferrihydrite sample (λ=785nm) contains weak features that may be consistent with a maghemite component (**Figure 3**). Maghemite has been reported as an

intermediate product during the transformation of ferrihydrite to hematite (Mazzetti and Thistlethwaite, 2002), thus it is possible that our sample also underwent partial transformation in addition to losing adsorbed anions. We note that Mazzetti and Thistlethwaite (2002) reported loss of SO_4^{2-} Raman peaks during prolonged measurement of scwhertmannite (a ferric oxyhydroxysulfate), providing another example of sulfate decomposition during Raman acquisitions, and transformation to maghemite then hematite.

The loss of the PO_4^{3-} peak in the 532 nm data, and its weakening in the 785nm data, is more puzzling as Rampe et al. (2016) reported no phosphate gas released within temperature range of their EGA measurements (<1150 °C). It is unclear whether our ferrihydrite samples would have reached high enough laser-induced temperatures to decompose or transform the adsorbed phosphate. However, we note that the PO_4^{3-} features were much weaker than the SO_4^{2-} features in the allophane Raman acquisitions, thus presumably the PO_4^{3-} features would be easier to obscure if any type of thermal modification occurred.

4.2 Applicability to Mars2020 and ExoMars data

The X-ray amorphous phases allophane, ferrihydrite and amorphous ferric sulfate (**Figure 1**), each have unique spectral features that can be used to identify them using Raman spectroscopy (**Figure 2**). Though amorphous materials have generally lower Raman cross-sections than crystalline materials (making them potentially difficult to detect in mineral mixtures), they may be distinguishable in cases where amorphous materials make up the bulk of the measurement footprint. Given that such a substantial fraction of the materials could be amorphous (based on XRD measurements at Gale crater, **Section 1**), there are likely to be many SuperCam and ExoMars observations in which amorphous phases dominate the Raman signal rather than being obscured by peaks from crystalline phases.

In the VNIR, hydration features at ~1.4 and ~1.9 μm are present in all samples, but appear more asymmetric and shifted to slightly longer wavelengths in the amorphous ferric sulfate sample (**Figure 4**). If measured in isolation, for example, with ExoMars MicrOmega (Bibring et al., 2017), it would likely be possible to distinguish allophane, ferrihydrite and amorphous ferric sulfate from one another. However if measured within a mixture, the diagnostic differences at wavelengths below ~1.5 μm would likely be obscured by other iron-bearing phases. Thus,

Raman spectroscopy is likely to be the best way to detect and distinguish between amorphous phases at Jezero crater and Oxia Planum, the landing sites for the Mars2020 and ExoMars rovers.

The power of Raman to detect adsorbed species is unique compared to remote IR spectroscopic methods, and may prove to be a major benefit in understanding the measured chemistry of Martian soils. On Earth, adsorption on mineral surfaces may have played a major role in prebiotic reactions and chemistry (e.g. Schoonen et al., 2004; Hazen, 2006) and thus the potential to characterize mineral surfaces in Martian soils and rocks might provide a new understanding of potential pathways for any microbial beginnings on Mars. Among potential sulfur-bearing amorphous species, we showed that Raman spectroscopy can be used to distinguish between amorphous ferric sulfate and adsorbed sulfate on allophane, with a strong spectral signal from the adsorbed sulfate anions (**Figures 2**). Adsorbed phosphate on allophane is also detectable with Raman. However, the same adsorbed species could not be detected on ferrihydrite, suggesting possible loss of these anions during the Raman acquisition (**Section 4.1**). More studies are needed to better understand the Raman detectability of different inorganic and organic adsorbed species on different soil components and the potential to alter or remove the adsorbed species during measurement.

One important issue related to Raman analysis of amorphous/nanophase materials is the potential for phase transformation during the data acquisition. Specifically, some nanophase iron oxides are notorious for transformation during Raman (532nm) acquisitions, even under low laser power (e.g. Hanesch, 2009). For example, goethite and ferrihydrite have been observed to convert to hematite, and magnetite to maghemite (Li et al., 2012; Sklute et al., 2018); we observed this in our own Raman spectra of ferrihydrite. With a continuous wave Raman system, this problem can be overcome using hundreds of short-duration (<1 s) accumulations at low power (<1 mW) (e.g. Sklute et al., 2018). We speculate that the pulsed-laser, time-resolved Raman system of SuperCam might permit avoidance of this issue. Though Fau et al. (2019) did investigate the potential for mineral transformation or structural damage with SuperCam and observed little evidence for transformations, they did not include nanophase ferric oxides other than hematite, or other amorphous phases, in their study. More work is needed to assess the behavior of other nanophase/amorphous materials under a time-resolved Raman system to understand whether these phases are likely to be detectable on Mars.

5. Conclusions

1. The following phases were synthesized and characterized with Raman spectroscopy using three different excitation energies (325, 532, 785 nm): amorphous ferric sulfate, allophane with and without adsorbed sulfate and phosphate anions, ferrihydrite with and without adsorbed phosphate anions. With the exception of amorphous ferric sulfate, all of these phases were also characterized with VNIR reflectance spectroscopy.

2. Adsorbed sulfate and phosphate anions were Raman-detectable on allophane but not on ferrihydrite. The lack of detection of adsorbed species on ferrihydrite is not fully understood, but one plausible explanation is that the species were decomposed under laser illumination during the Raman acquisition (**Section 4.1**).

As previously shown by Rampe et al. (2016) for these phases, adsorbed species were not detectable in the VNIR.

3. Raman spectroscopy can be used to distinguish between two candidate sulfur-bearing amorphous phases: amorphous ferric sulfate and allophane with adsorbed sulfate anions.

4. Using the 532 nm excitation, ferrihydrite was converted to hematite during Raman acquisition. We were unable to acquire a ferrihydrite signal using lower laser power and longer integrations. Phase transformations are a potential concern for remote Raman measurements, however, the pulsed-laser style of Raman acquisition that will be used by Mars2020 SuperCam may reduce this effect. More work is needed to understand the resistance to phase transformations of amorphous and nano-crystalline materials under a pulsed-laser Raman system.

Acknowledgements

This work was supported by the NASA Solar System Workings program (80NSSC18K0535) and the Planetary Major Equipment Program (80NSSC18K0516). We thank Tae Jin Kim for assistance with the Renishaw Raman measurements, Donald Hendrix for assistance with the ICP, and Laura Breitenfeld for assistance with the micro-Raman measurements.

Data Availability Statement

All Raman, VNIR and XRD data produced in this work will be made publicly available in Gregerson et al., (2020) [a Zenodo repository at 10.5281/zenodo.4289411].

References

Achilles, C. N., et al. (2017), Mineralogy of an active eolian sediment from the Namib dune,

494 Gale crater, Mars, J. Geophys. Res. Planets, 122, 2344–2361,
495 doi:10.1002/2017JE005262.
496 Achilles, C. N., Rampe, E. B., Gabriel, T. S. J., Ming, D. W., Morris, R. V, Sutter, B., et al.
497 (2020). Factors Influencing the Formation and Abundance of X-Ray Amorphous
498 Materials Detected in Gale Crater Mudstones and Sandstones. 51st Lunar and Planetary
499 Science Conference.
500 Bandfield, J. L. (2002), Global mineral distributions on Mars, J. Geophys. Res., 107(E6), 5042.
501 Beegle, L., Bhartia, R., White, M., Deflores, L., Abbey, W., Wu, Y. H., et al. (2015).
502 SHERLOC: Scanning habitable environments with Raman & luminescence for organics
503 & chemicals. IEEE Aerospace Conference Proceedings, 2015-June, 1–11.
504 https://doi.org/10.1109/AERO.2015.7119105
505 Bell, J. F., R. V. Morris, J. B. Adams (1993). Thermally Altered Palagonitic Tephra - a Spectral
506 and Process Analog to the Soil and Dust of Mars. *Journal of Geophysical Research-Planets*
507 *98(E2):* 3373-3385.
508 Bibring, J.-P., Hamm, V., Pilorget, C., Vago, J.L., and the MicrOmega Team (2017), The
509 MicrOmega Investigation onboard ExoMars, Astrobiology, 17, 6-7, 621-626.
510 Bishop, J. L., Rampe, E. B., Bish, D. L., Abidin, Z., Baker, L. L., Matsue, N., & Henmi, T.
511 (2013). Spectral and hydration properties of allophane and imogolite. Clays and Clay
512 Minerals, 61(1), 57–74. https://doi.org/10.1346/CCMN.2013.0610105.
513 Bish, D.L., et al., 2013. X-ray diffraction results from Mars Science Laboratory: mineralogy of
514 Rocknest at Gale Crater. Science 341. 1238932–1238932 doi: 10.1126/science.1238932.
515 Bishop, J. L., Rampe, E. B., Bish, D. L., Abidin, Z., Baker, L. L., Matsue, N., & Henmi, T.
516 (2013). Spectral and hydration properties of allophane and imogolite. Clays and Clay
517 Minerals, 61(1), 57–74. https://doi.org/10.1346/CCMN.2013.0610105
518 Blake, D.F., et al., 2013. Curiosity at Gale Crater, Mars: characterization and analysis of the
519 Rocknest sand shadow. Science 341. 1239505–1239505 doi: 10.1126/science.1239505.
520 Cannon, K. M. J. F. Mustard, S. W. Parman, E. C. Sklute, M. D. Dyar, R. F. Cooper (2017),
521 Spectral properties of Martian and other planetary glasses and their detection in remotely
522 sensed data, *JGR-Planets*, *122*, 249-268.
523 Carey, C., Dyar, M. D., Boucher, T., & Giguere, S. (2017). Web-Based Software for
524 Preprocessing, Matching, Fitting, Prediction, and Visualization of Spectroscopic Data: The
525 Data Exploration, Visualization, and Analysis of Spectra (DEVAS) Website. *Lunar and*
526 *Planetary Sci. XLVIII* (Abs. 1097).
527 Dahlgren, RA, M Saigusa, and FC Ugolini (2004), The nature, properties and management of
528 volcanic soils, Adv. in Agronomy, 82, 113-182, 10.1016/S0065-2113(03)82003-5
529 Das, S., & Hendry, M. J. (2011). Application of Raman spectroscopy to identify iron minerals
530 commonly found in mine wastes. Chemical Geology, 290(3–4), 101–108.
531 https://doi.org/10.1016/j.chemgeo.2011.09.001.
532 Dehouck, E., McLennan, S.M., Meslin, P.-Y., Cousin, A., 2014. Constraints on abundance,
533 composition, and nature of X-ray amorphous components of soils and rocks at Gale crater,
534 Mars. J. Geophys. Res. Planets. 119, 2640–2657. doi: 10.1002/2014JE004716.
535 Dehouck, E., McLennan, S. M., Sklute, E. C., & Dyar, M. D. (2017). Stability and fate of
536 ferrihydrite during episodes of water/rock interactions on early Mars: An experimental
537 approach. Journal of Geophysical Research: Planets, 122(2), 358–382.
538 https://doi.org/10.1002/2016JE005222
539 Dyar, M. D., Giguere, S., Carey, C. J., & Boucher, T. (2016). Comparison of baseline removal

methods for laser-induced breakdown spectroscopy of geological samples. Spectrochimica Acta - Part B Atomic Spectroscopy, 126, 53–64. https://doi.org/10.1016/j.sab.2016.10.018

Farrand, W. M., S. P. Wright, A. D. Rogers, T. D. Glotch (2016), Basaltic glass formed from hydrovolcanism and impact processes: Characterization and clues for detection of mode of origin from VNIR through MWIR reflectance and emission spectroscopy, *Icarus, 275*, 16–28, doi:10.1016/j.icarus.2016.03.027.

Fau, A., Beyssac, O., Gauthier, M., Meslin, P. Y., Cousin, A., Benzerara, K., et al. (2019). Pulsed laser-induced heating of mineral phases: Implications for laser-induced breakdown spectroscopy combined with Raman spectroscopy. Spectrochimica Acta - Part B Atomic Spectroscopy, 160(2019), 105687. https://doi.org/10.1016/j.sab.2019.105687

Gálvez, N., Barrón, V., and Torrent, J. (1999) Effect of phosphate on the crystallization of hematite, goethite, and lepidocrocite from ferrihydrite. Clays and Clay Minerals, 47, 304–311.

Glotch, T. D., Bandfield, J. L., et. al. (2006), Mineralogy of the light-toned outcrop at Meridiani Planum as seen by the Miniature Thermal Emission Spectrometer and implications for its formation: *Journal of Geophysical Research-Planets, v. 111*, E12S03.

Gregerson et al. (2020) [Data set] will be added once article is near acceptance for publication.

Hanesch, M. (2009). Raman spectroscopy of iron oxides and (oxy)hydroxides at low laser power and possible applications in environmental magnetic studies. Geophysical Journal International, 177(3), 941–948. https://doi.org/10.1111/j.1365-246X.2009.04122.x

Hazen RM. 2006. Mineral surfaces and the prebiotic selection and organization of biomolecules. Am Mineral 91:1715–1729.

Horgen, B. and Bell, J.F. (2012). Widespread weathered glass on the surface of Mars. Geology 40(5), 391-394. DOI: 10.1130/G32755.1.

Leshin, L.A., et al., 2013. Volatile, isotope, and organic analysis of Martian fines with the Mars Curiosity Rover. Science 341. UNSP 1238937 doi: 10.1126/science. 1238937.

Li Y-S, Church JS, Woodhead AL (2012) Infrared and Raman spectroscopic studies on iron oxide magnetic nano-particles and their surface modifications. J Magnetism & Magnetic Materials 324:1543–1550

Ling, Z. C., & Wang, A. (2010). A systematic spectroscopic study of eight hydrous ferric sulfates relevant to Mars. Icarus, 209(2), 422–433. https://doi.org/10.1016/j.icarus.2010.05.009.

Mazzetti, L., & Thistlethwaite, P. J. (2002). Raman spectra and thermal transformations of ferrihydrite and schwertmannite. Journal of Raman Spectroscopy, 33(2), 104–111. https://doi.org/10.1002/jrs.830

McAdam, A.C., et al., 2014. Sulfur-bearing phases detected by evolved gas analysis of the Rocknest aeolian deposit, Gale Crater, Mars: Rocknest sulfur phases detected by SAM. J. Geophys. Res. Planets 119, 373–393. doi: 10.1002/2013JE0 04518.

Michalski, J. R., M. D. Kraft, T. G. Sharp, L. B. Williams, and P. R. Christensen (2005), Mineralogical constraints on the high-silica martian surface component observed by TES, *Icarus, 174(1)*, 161–177.

Milliken, R. E. et al. (2008), Opaline silica in young deposits on Mars, *Geology, 36(11)*, 847, doi:10.1130/G24967A.1.

Novak, P., Ocenasek, J., Prusakova, L., Vavrunkova, V., Savková, J., & Rezek, J. (2016). Influence of heat generated by a Raman excitation laser on the structural analysis of thin amorphous silicon film. Applied Surface Science, 364, 302–307.

https://doi.org/10.1016/j.apsusc.2015.12.091
Ohashi, F., Wada, S.-I., Suzuki, M., Maeda, M., and Tomura, S. (2002) Synthetic allophane from high-concentration solutions: Nanoengineering of the porous solid. Clay Minerals, 37, 451–456.
Rampe, E. B., M. D. Kraft, T. G. Sharp, D. C. Golden, D. W. Ming, and P. R. Christensen (2012), Allophane detection on Mars with Thermal Emission Spectrometer data and implications for regional-scale chemical weathering processes, *Geology, 40*, 995-998 doi:10.1130/G33215.1.
Rampe, E. B., Morris, R. V., Archer, P. D., Agresti, D. G., & Ming, D. W. (2016). Recognizing sulfate and phosphate complexes chemisorbed onto nanophase weathering products on Mars using in-situ and remote observations k. American Mineralogist, 101, 678–689.
Rampe, E. B., Ming, D. W., Blake, D. F., Bristow, T. F., Chipera, S. J., Grotzinger, J. P., et al. (2017). Mineralogy of an ancient lacustrine mudstone succession from the Murray formation, Gale crater, Mars. Earth and Planetary Science Letters, 471, 172–185. https://doi.org/10.1016/j.epsl.2017.04.021
Rampe, E. B., Bristow, T. F., Morris, R. V, Morrison, S. M., Achilles, C. N., Ming, D. W., et al. (2020). Mineralogy of Vera Rubin Ridge in Gale Crater from the Mars Science Laboratory CheMin Instrument. 51st Lunar and Planetary Science Conference.
Rice, M. S., Cloutis, E. a., Bell, J. F., Bish, D. L., Horgan, B. H., Mertzman, S. a., et al. (2013). Reflectance spectra diversity of silica-rich materials: Sensitivity to environment and implications for detections on Mars. Icarus, 223(1), 499–533. https://doi.org/10.1016/j.icarus.2012.09.021
Ruff, S. W. et al. (2011), Characteristics, distribution, origin, and significance of opaline silica observed by the Spirit rover in Gusev crater, Mars, *J. Geophys. Res., 116*, E00F23, doi:10.1029/2010JE003767.
Rull, F., Maurice, S., Hutchinson, I., Moral, A., Perez, C., Diaz, C., et al. (2017). The Raman Laser Spectrometer for the ExoMars Rover Mission to Mars. Astrobiology, 17(6–7), 627–654. https://doi.org/10.1089/ast.2016.1567
Schoonen MAA, Smirnov A, Cohn C. 2004. A perspective on the role of minerals in prebiotic synthesis. Ambio 33: 539 – 551.
Schwertmann, U., and Cornell, R.M. (2000) Iron Oxides in the Laboratory: Preparation and characterization, 188 p. Wiley-VCH, Weinheim, Germany.
Sklute, E. C., H. Jensen, A. D. Rogers, and R. J. Reeder (2015), Morphological, Structural, and Spectral Characteristics of Amorphous Iron Sulfates, *JGR-Planets, 120(4)*, 809-830 DOI: 10.1002/2014JE004784.
Sklute, E. C., Kashyap, S., Dyar, M. D., Holden, J. F., Tague, T., Wang, P., & Jaret, S. J. (2018a). Spectral and morphological characteristics of synthetic nanophase iron (oxyhydr) oxides. Physics and Chemistry of Minerals, 45(1), 1–26. https://doi.org/10.1007/s00269-017-0897-y
Tarcea, N., Harz, M., Rösch, P., Frosch, T., Schmitt, M., Thiele, H., et al. (2007). UV Raman spectroscopy-A technique for biological and mineralogical in situ planetary studies. Spectrochimica Acta - Part A: Molecular and Biomolecular Spectroscopy, 68(4), 1029–1035. https://doi.org/10.1016/j.saa.2007.06.051.
Vaniman, D.T., Bish, D.L., Chipera, S.J., Fialips, C.I., Carey, J.W., Feldman, W.C., 2004. Magnesium sulphate salts and the history of water on Mars. Nature 431, 663– 665. doi: 10.1038/nature02973.

Wada, K. (1987) Minerals formed and mineral formation from volcanic ash by weathering. Chemical Geology, 60,17-28.

Wang, A., & Zhou, Y. (2014). Experimental comparison of the pathways and rates of the dehydration of Al-, Fe-, Mg- and Ca-sulfates under Mars relevant conditions. Icarus, 234, 162–173. https://doi.org/10.1016/j.icarus.2014.02.003

Wang, A., J. J. Freeman, and B. L. Jolliff (2009), Phase transition pathways of the hydrates of magnesium sulfate in the temperature range 50 degrees C to 5 degrees C: Implication for sulfates on Mars, J. *Geophys. Res.*, *114*, doi:10.1029/2008JE003266.

Wang, A., Ling, Z., Freeman, J. J., & Kong, W. (2012). Stability field and phase transition pathways of hydrous ferric sulfates in the temperature range 50°C to 5°C: Implication for martian ferric sulfates. Icarus, 218(1), 622–643.

Wartewig, S. (2003) IR and Raman Spectroscopy: Fundamental Processing, Wiley, (175 pp.)

Wiens, R. C., Maurice, S., & Perez, F. R. (2017). The SuperCam Remote Sensing Instrument Suite for the Mars 2020 Rover: A Preview. Spectroscopy, 32(5), 50–55. Retrieved from http://www.spectroscopyonline.com/supercam-remote-sensing-instrument-suite-mars-2020-rover-preview

Xi, Zhang, Luan, Du, Li, Liang, et al. (2019). Micro-Raman Study of Thermal Transformations of Sulfide and Oxysalt Minerals Based on the Heat Induced by Laser. *Minerals*, 9(12), 751. https://doi.org/10.3390/min9120751

Xu, W., Tosca, N.J., McLennan, S.M., Parise, J.B., 2009. Humidity-induced phase transitions of ferric sulfate minerals studied by in situ and ex situ X-ray diffraction. Am. Mineral. 94, 1629–1637. doi: 10.2138/am.2009.3182.